Research on DC resistivity for an arbitrarily anisotropic earth using circular scanning measurement

Zhilong Yang* *Jilin University, Changchun, China, zhilongyang_2015@163.com*
Changchun Yin *Jilin University, Changchun, China, yinchangchun@jlu.edu.cn*
Xiuyan Ren *Jilin/RMIT University, Melbourne, Australia, jdrxy@hotmail.com*
Changkai Qiu *Jilin University, Changchun, China, qiuchangkai@hotmail.com*
Xiaoyue Cao *Jilin University, Changchun, China, caoxy_em@163.com*

SUMMARY

This paper presents a 3D forward modelling algorithm with an adaptive finite-element method based on unstructured grids that when used with a circular scanning DC measurement technique can provide an indication of anisotropy in a layered earth. The accuracy of this algorithm is checked against 1D semi-analytical solutions for an arbitrarily anisotropic earth. This anisotropy produces a measurement paradox, results are dependent on the physical relationship between DC transmitter and receiver. To resolve this paradox, a circular scanning measurement technique has been suggested. Through analysing the response of typical anisotropic models, we study the characteristics of apparent resistivity related to the electrically anisotropic media and identification of underground electrical anisotropy. The results of numerical experiments shows the effectiveness of our algorithm and the analysis will be helpful to the interpretation of anisotropic DC resistivity data.

Key words: numerical modelling, unstructured grids, local adaptive finite-element method, electrical anisotropy, circular scanning measurement

INTRODUCTION

The direct current (DC) resistivity method has been widely used in the exploration of subsurface minerals, hydrogeology survey and environmental & engineering investigations for years (Xu et al, 1994). The method can predict the resistivity distribution of the subsurface structures through the distribution of the apparent resistivity observed on the ground (Pain et al, 2003). The electrically isotropic models are widely used in existing forward and inversion algorithms. However, using an isotropic model to interpret the data from an anisotropic earth will cause big mistakes (Yin & Weidelt, 1999), especially when there are distinct stratifications or fractures, or directional structures in the earth. Therefore, in areas with distinct anisotropy the DC resistivity modelling should take into account the electrical anisotropy (Yin & Weidelt, 1999; Yin, 2000).

The analytical solutions of the resistivity response for a transversely isotropic uniform half-space are known (Habberjam, 1975), as are solutions for anisotropic layered media (Wait, 1990; Li & Uren, 1997; Yin & Maurer, 2001). For complicated anisotropic media, the present numerical algorithms include the volume integral methods (Li & Uren, 1998), the finite-difference methods (Wang & Fang, 2001), the finite-element methods (Wang & Wu, 2013), and the spectral element methods (Zhou et al, 2009). Li et al (1997) modelled the arbitrarily anisotropic subsurface using integral equation method, and Wang et al (2013) modelled the resistivity response of anisotropic bodies embedded by isotropic rocks using a finite-element method.

In traditional DC resistivity prospecting, the observation data only contains one-directional resistivity information, the resistivity in other directions is neglected. Therefore the interpretation of the observation data cann't accurately predict the subsurface structures because of the existence of an anisotropic paradox in the determination of the apparent resistivity (Yin & Weidelt, 1999). In order to solve the measurement problem, Yin et al. (2016) proposed a circular scanning measurement technique and validated the method using a one-dimensional layered model of an anisotropic medium. By plotting apparent resistivity as a polar diagram, any subsurface anisotropy could be recognized easily.

In this paper, we present an adaptive finite-element method based on unstructured grids to model the arbitrarily anisotropic media. To guarantee the computational accuracy in the regions near the source and with high resistivity contrasts, we adopted the local adaptive grids refinement technique based on the gradient recovery theory. This technique has a smaller memory requirement but fast computational speed than the global adaptive refinement algorithm in IAG (Zhengyong Ren, 2010). It can improve the mesh adaptive flexibility by setting deviation thresholds for different areas. Furthermore, a circular scanning measurement has been suggested in the simulation of the 3-D subsurface structures. We set the transmitter in the centre of a detecting region, and the survey points are positioned circularly with same distance to the transmitter. By changing the distance to the transmitter, we can get more information on the resistivity distribution and anisotropy at different depths of the earth.

METHOD AND RESULTS

The boundary value problem

For the arbitrarily anisotropic subsurface models, the conductivity tensor $\sigma = \rho^{-1}$ or resistivity vector ρ can be expressed by a symmetric tensor with 6 individual components:

$$\boldsymbol{\sigma}=\begin{pmatrix}\sigma_{xx} & \sigma_{xy} & \sigma_{xz}\\ \sigma_{yx} & \sigma_{yy} & \sigma_{yz}\\ \sigma_{zx} & \sigma_{zy} & \sigma_{zz}\end{pmatrix}. \tag{1}$$

The relationship between the conductivity tensor and the principal conductivity$\boldsymbol{\sigma}_c$ tensor is (Yin, 1999)

$$\boldsymbol{\sigma}=\boldsymbol{R}^{\mathrm{T}}\boldsymbol{\sigma}_{\mathrm{c}}\boldsymbol{R}\,, \tag{2}$$

where T represents the matrix transpose, $\boldsymbol{R}=\boldsymbol{R}_x\boldsymbol{R}_y\boldsymbol{R}_z$ is the Euler rotation matrix.

In the 3-D domain Ω, the potential $u=u^{\mathrm{s}}+u^{\mathrm{p}}$ (u^{s} is the secondary potential and u^{p} is the primary potential) induced by the point current source satisfies the Poisson equation, the potentials on the ground boundary Γ_0 satisfies the Newman boundary condition and the potentials in the infinite Γ_∞ satisfy the hybrid boundary condition. Therefore, the boundary value problem for the secondary potential u^{s} can be written as

$$\nabla\cdot\left(\boldsymbol{\sigma}\cdot\nabla u^{\mathrm{s}}\right)=-\nabla\cdot\left(\left(\boldsymbol{\sigma}-\boldsymbol{\sigma}_0\right)\cdot\nabla u^{\mathrm{p}}\right),\qquad \boldsymbol{r}\in\Omega\,. \tag{3}$$

$$\nabla u^{\mathrm{s}}\cdot\boldsymbol{n}=-\nabla u^{\mathrm{p}}\cdot\boldsymbol{n}\,,\qquad \boldsymbol{r}\in\Gamma_0\,. \tag{4}$$

$$\boldsymbol{\sigma}\cdot\nabla u^{\mathrm{s}}\cdot\boldsymbol{n}=-\frac{\boldsymbol{n}\cdot\boldsymbol{r}}{\boldsymbol{B}}u^{\mathrm{s}}-\boldsymbol{\sigma}\cdot\nabla u^{\mathrm{p}}\cdot\boldsymbol{n}-\frac{\boldsymbol{n}\cdot\boldsymbol{r}}{\boldsymbol{B}_{\mathrm{p}}}u^{\mathrm{p}}\,,\quad \boldsymbol{r}\in\Gamma_\infty\,. \tag{5}$$

The analytical solution of primary singular field is

$$u^{\mathrm{p}}=\frac{I}{4\pi\left|\boldsymbol{\sigma}_0\right|^{1/2}}\frac{1}{\sqrt{\boldsymbol{B}_{\mathrm{p}}}}\,, \tag{6}$$

where $\boldsymbol{B}_{\mathrm{p}}=\boldsymbol{r}^{\mathrm{T}}\cdot\boldsymbol{\sigma}_0^{-1}\cdot\boldsymbol{r}$, $\boldsymbol{\sigma}_0$ is the conductivity tensor of the surrounding rock.

We set a test function $\boldsymbol{N}$ in the Hilbert domain $\mathbf{H}^1(\Omega)$ and obtain the following equation with the Galerkin finite-element methods:

$$\iiint_{\Omega}\left(\nabla\cdot\left(\boldsymbol{\sigma}\cdot\nabla u^{\mathrm{s}}\right)+\nabla\cdot\left(\left(\boldsymbol{\sigma}-\boldsymbol{\sigma}_0\right)\cdot\nabla u^{\mathrm{p}}\right)\right)\boldsymbol{N}\mathrm{d}\Omega=0\,. \tag{7}$$

The modelling domain is then discretized into a set of tetrahedral elements with the open-source mesh generator Tetgen (Si. 2006). We combine the boundary conditions with equation 9 and simplify it via the Green's identities and obtain

$$\boldsymbol{K}\boldsymbol{U}^{\mathrm{s}}=\boldsymbol{b}\,, \tag{8}$$

where $\boldsymbol{K}$ is the global coefficient matrix, $\boldsymbol{b}$ is the source term, $\boldsymbol{U}^{\mathrm{s}}$ is the secondary potential vector to be solved. In this way, we can obtain the secondary potential from the large sparse linear equations by using the parallel direct solver MUMPS and get the apparent resistivity from the total field potential that is the sum of the primary potential and the secondary potential.

Local adaptive mesh refinement

In 1987, Zienkiewicz proposed a posteriori error estimation algorithm (which is called z-z method) based on gradient recovery technique. The method which is independent in specific problems is simple and efficient, so it is easy to transplant it to unstructured grids.

In the L_2 norm, the element relative error of the 3-D statics electromagnetic field in the finite-element simulation is as follows:

$$\left\|e\right\|_i=\left[\int_{\Omega_i}\left(\mathrm{d}u-\nabla u^{\mathrm{F}}\right)^{\mathrm{T}}\left(\mathrm{d}u-\nabla u^{\mathrm{F}}\right)\mathrm{d}\Omega\right]^{1/2}\qquad i=1,2,3\cdots,n.\,, \tag{9}$$

where i is the number of the element, n is the total number of the elements discretized in the simulating region, Ω_i is the real sapce of each element, ∇u^{F} is the potential gradient. The element recovery gradient du is obtained by the super-convergent patch recovery technique that can be written as

$$\mathrm{d}u=\boldsymbol{G}\boldsymbol{a}\,, \tag{10}$$

where

$$\boldsymbol{G}=\begin{bmatrix}1\\ x\\ y\\ z\end{bmatrix}^{\mathrm{T}}\;;\quad \boldsymbol{a}=\begin{bmatrix}a_{0x} & a_{0y} & a_{0z}\\ a_{1x} & a_{1y} & a_{1z}\\ a_{2x} & a_{2y} & a_{2z}\\ a_{3x} & a_{3y} & a_{3z}\end{bmatrix}. \tag{11}$$

Where $\boldsymbol{a}$ is a matrix of unknown parameters (Zhengyong Ren, 2010). And the element gradient recovery can be obtained by $\boldsymbol{a}$ in the element patch that contains all the elements adjoining the element domain Ω_i. After that, we can obtain the element relative error $\|e\|_i$ through the equation 9.

In the adaptive mesh refinement strategy, we first set the maximum error threshold for each target region:

$$\left\|e\right\|_j\;,\ j=1,2\cdots,k.\,, \tag{12}$$

where k is the number of the target regions. The volume of each element can be adjusted by the element relative error and the maximum threshold. The adjusted element volume is

$$V_i = V_i^* \frac{\|e\|_j}{\|e\|_i}, \tag{13}$$

where V_i^* is the element volume before each iteration. After obtaining the new volume of each element, we can regenerate the new grid by Tetgen. We repeat the above steps until the element relative error is smaller than the threshold.

Accuracy verification

We will demonstrate the accuracy of our algorithm by simulating a two-layer anisotropic model shown in Figure 1. The principal resistivity and the Euler rotation angles of the first layer are respectively ρ_{x1} =ρ_{L1}=100 Ω·m, ρ_{y1}=ρ_{L1}=100 Ω·m, ρ_{z1}=ρ_{T1}=400 Ω·m, α_1=0°, β_1=90°, γ_1=0°. For the second layer, they are ρ_{x2}=ρ_{L2}=10 Ω·m, ρ_{y2}=ρ_{L2}=10 Ω·m, ρ_{z2}=ρ_{T2}=40 Ω·m, α_2=0°, β_2=90°, γ_2=0°. The accuracy verification is showed in Figure 2. By analysing the result we can see: 1) the algorithm of this paper has a high modelling accuracy.

2) When the offset *r* between the transmitter and the receiver starts at 0, the plots in Figure 2 a and c mainly show the resistivity of the first layer. However, the value in Figure 2 a does not equal c. Figure 2 a shows the apparent resistivity in *x*-direction with a value equals to ρ_{L1}=100 Ω·m, which is the resistivity along the stratification of the first layer. Figure 2 a shows the apparent resistivity in *y*-direction and the value equals to $\rho_{M1} = \sqrt{\rho_{L1}\rho_{T1}}$ =200 Ω·m that is the geometric mean of the resistivity along the stratification of the first layer ρ_{L1} and the resistivity perpendicular to the stratification of the first layer ρ_{T1}. When the offset *r* becomes large enough, the value of Figure 2 a and c stay invariant that shows the resistivity of the second layer. The results are similar to the first layer: the apparent resistivity in *x*-direction is ρ_{L2}=10 Ω·m while that in *y*-direction is $\rho_{M2} = \sqrt{\rho_{L2}\rho_{T2}}$ =20 Ω·m. These results typify the measurement paradox that occurs when measuring apparent resistivity in an anisotropic layered earth; the apparent resistivity is perpendicular to the distribution of the true earth resistivity.

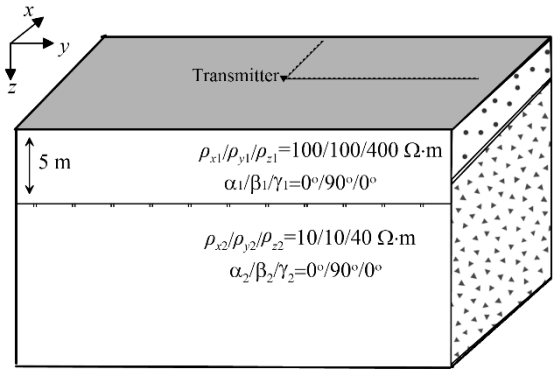

Figure 1: A two-layer model

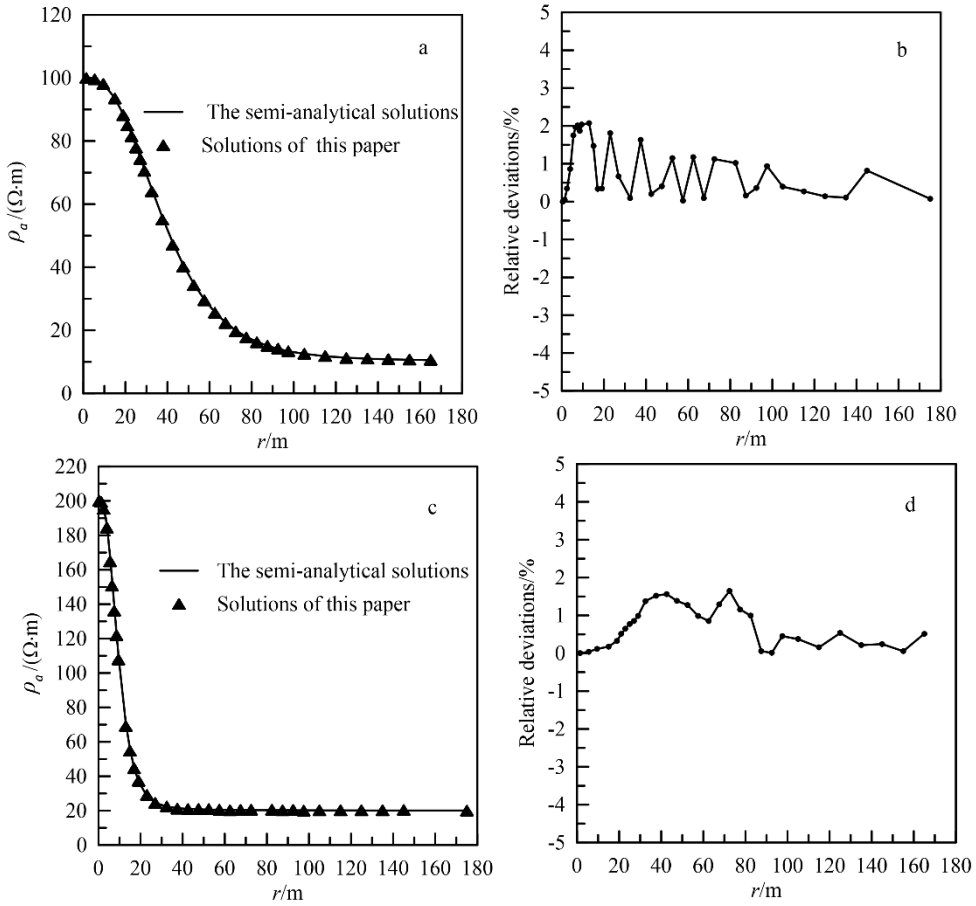

Figure 2: Comparisons of the result computed by this paper with semi-analytical solutions and the relative deviations a,b is around the *x* direction; c,d is around the *y* direction, *r* is the offset.

Modelling of an arbitrarily anisotropic half-space

Figure 3 shows the apparent resistivity distribution of an arbitrarily anisotropic half-space whose principal resistivity is $\rho_{x0}/\rho_{y0}/\rho_{z0}$=100/400/100 Ω·m, and the results are calculated for a circular scanning survey (refer to Figure 4). In Figure 3 a, the principal resistivity is rotated around the *z* axis. From the polar plots we can see that the shape of the apparent resistivity is similar to an ellipse: it is stretched in the direction of the low principal resistivity, and the value (elliptic long axis) equals to the geometric mean of the principal resistivity in the *x* and the *y* direction; while it is compressed in the direction of the high principal resistivity. The value (elliptic short axis) equals to the principal resistivity in the *x* direction. This results correspond to the above discussed anisotropic paradox. This implied that via the anisotropic paradox of apparent resistivity we can distinguish the anisotropic characteristics of the underground media. In Figure 3 b, the principal resistivity is rotated around the *x* axis. We can see that before the rotation (α=0°), the apparent resistivity of the anisotropic half-space is similar to the above apparent resistivity distributions. When the anisotropic half-space is rotated around the *x* axis, the elliptic short axis turns to be stretched while the elliptic long axis stays invariant. When rotated 90° around the *x* axis, the model turns to be horizontal isotropic (at this point the principal resistivity in the *x* direction is the same as in the *y* direction). The polar plot becomes a circle with radius equals to the geometric mean $\rho_{\mathrm{M}} = \sqrt{\rho_{\mathrm{L}}\rho_{\mathrm{T}}} = \sqrt{\rho_x\rho_z} = \sqrt{\rho_y\rho_z}$ =200 Ω·m. Thus we can conclude that the anisotropic characteristics and the inclination of the strata of an anisotropic medium can be identified from the characteristics of the polar plot.

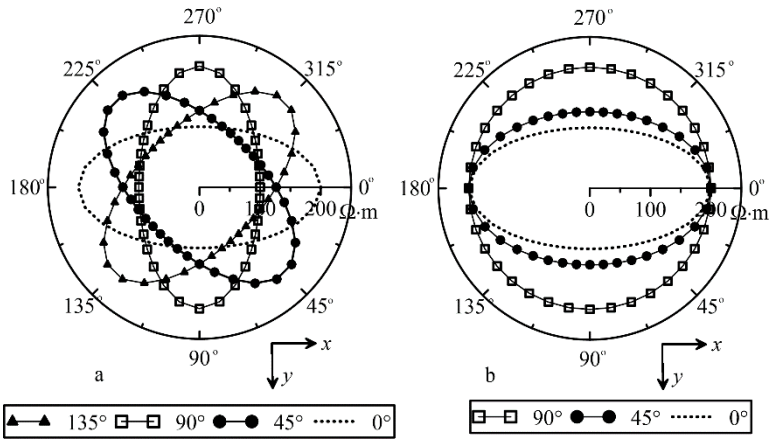

Figure 3: Polar plots of apparent resistivity for an anisotropic half-space
a. The principal resistivity of the half-space medium is rotated 0º, 45º, 90º, 135º around the *z* axis; b. the principal resistivity of the half-space medium is rotated 0º, 45º, 90º, 135º around the *x* axis.

Modelling of an arbitrarily anisotropic anomaly embedded by arbitrarily anisotropic rocks

We will study the characteristics of the apparent resistivity for an arbitrarily anisotropic anomalous body embedded by arbitrarily anisotropic rocks. Figure 4 shows the details of our model, the computational region is 2000 m×2000 m×1000 m and the extended region is 10000 m×10000 m×10000 m. The principal resistivity of the anomalous body is ρ_{x1}=10 Ω·m, ρ_{y1}=40 Ω·m, ρ_{z1}=10 Ω·m, while the principal resistivity of the surrounding rock is ρ_{x1}=100 Ω·m, ρ_{y1}=400 Ω·m, ρ_{z1}=100 Ω·m.

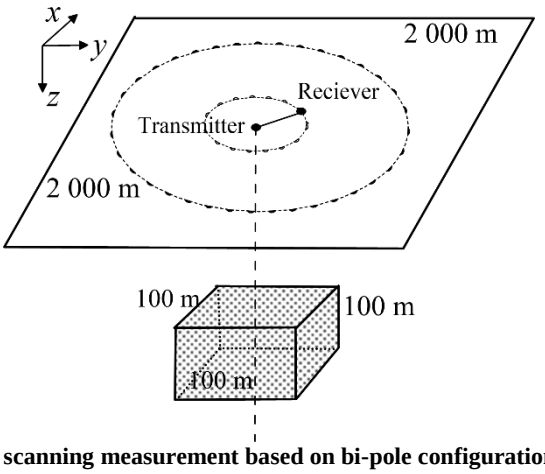

Figure 4: Circular scanning measurement based on bi-pole configuration over a 3D model

We set 600 m×600 m×600 m area as the computational region which contains the anomalous body and set the element relative error as 5% to refine the mesh. To get a high accuracy of the secondary potential, we further set the element relative error as 1% for two regions that include the anomalous body and a small region containing the transmitter. To show clearly the result of the local refinement, in Figure 5 we only show the *y*-*z* plane of a region which is 600 m×600 m×300 m. Comparing the three maps in Figure 5, we can see that after the third refinement of the volume elements, the element relative errors become smaller than the threshold in all target regions. The about 3% relative element error shown near the surface of the anomaly is caused by a large (1000%) resistivity contrast in this region.

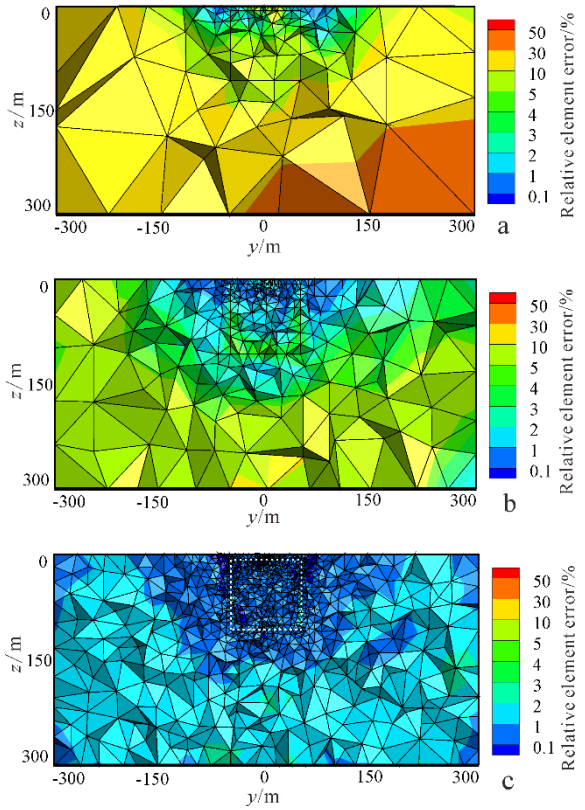

Figure 5: Local adaptive mesh refinement for 3-D model

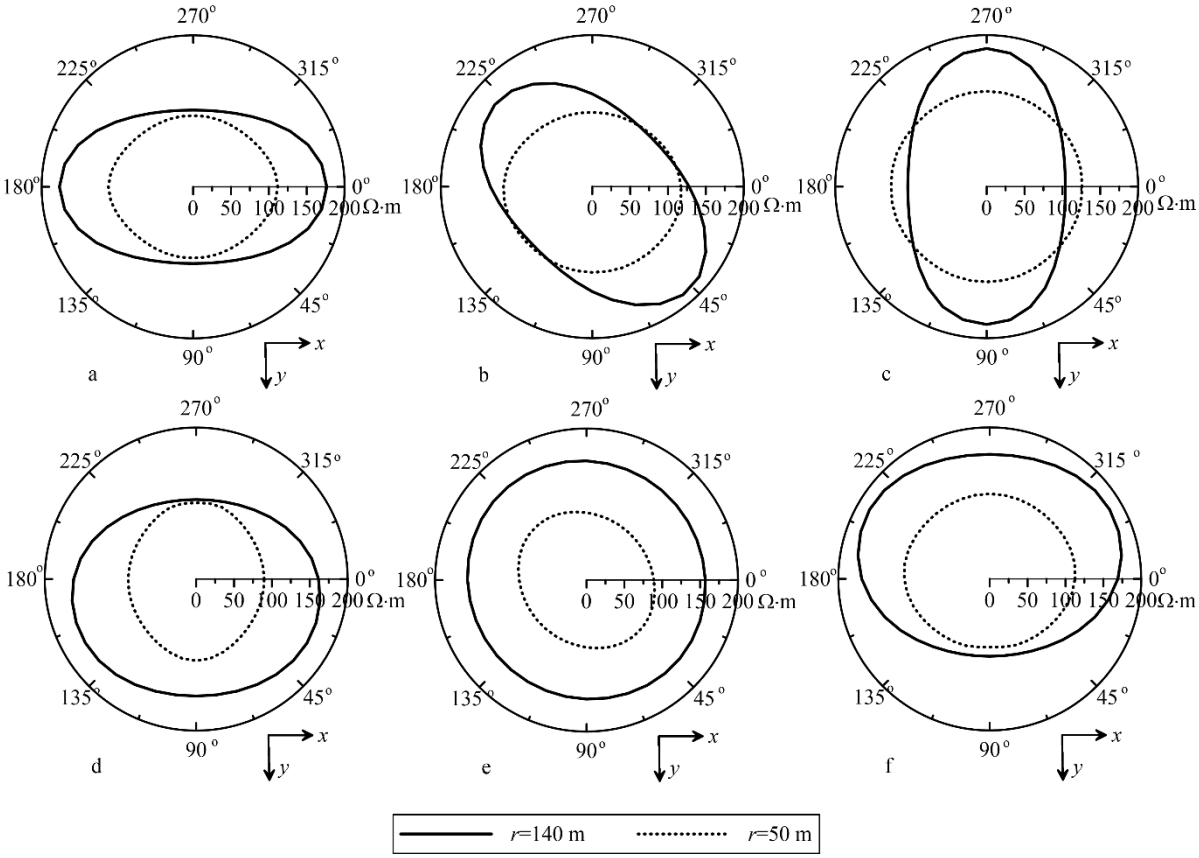

Figure 6: Polar plots of the apparent resistivity for an anisotropic abnormal body embedded in arbitrarily anisotropic surrounding rocks

The principal resistivity of the surrounding rocks is $\rho_{x0}/\rho_{y0}/\rho_{z0}$=100/400/100 Ω·m, and the principal resistivity of the anomaly is $\rho_{x1}/\rho_{y1}/\rho_{z1}$=10/40/10 Ω·m. The rotation angels of the surrounding rocks and the anomalous body in each map are: a.

$\alpha_0/\beta_0/\gamma_0$=0º/0º/0º, $\alpha_1/\beta_1/\gamma_1$=0º/0º/0º; b. $\alpha_0/\beta_0/\gamma_0$=0º/0º/45º, $\alpha_1/\beta_1/\gamma_1$=135º/0º/0º; c. $\alpha_0/\beta_0/\gamma_0$=0º/0º/90º, $\alpha_1/\beta_1/\gamma_1$=90º/0º/0º; d. $\alpha_0/\beta_0/\gamma_0$=45º/0º/0º, $\alpha_1/\beta_1/\gamma_1$=0º/0º/90º; e. $\alpha_0/\beta_0/\gamma_0$=90º/0º/0º, $\alpha_1/\beta_1/\gamma_1$=0º/0º/45º; f. $\alpha_0/\beta_0/\gamma_0$=135º/0º/0º, $\alpha_1/\beta_1/\gamma_1$=45º/0º/0º.

Figure 6 shows the modelling results for the anisotropic anomalous body embedded by homogeneous anisotropic rocks. Each figure in Figure 6 has two different polar plots respectively for offsets of 50 m (dotted line) and 140 m (solid line). From the figure, one sees that: 1) when the surrounding rocks are not dipping anisotropic, the distribution of apparent resistivity is symmetric, however, the anisotropic paradox still exists; 2) when the surrounding rocks are dipping anisotropic, the distribution of apparent resistivity is un-symmetric, with the smaller ellipsoid pointing toward the inclination of the stratification; 3) the apparent resistivity distribution for the abnormal body shows similar characteristics, only the anomaly is largely overwhelmed by surrounding rocks; 4) the anisotropic characteristics of the abnormal body and the surrounding can be distinguished from the apparent resistivity distribution for different offsets between transmitter and receiver.

CONCLUSIONS

In this paper, we conduct the 3-D DC resistivity simulation for an arbitrarily anisotropic model using finite-element method based on unstructured grids. The algorithm has a high accuracy when checked against 1D semi-analytical solutions for an arbitrarily anisotropic earth. We have modelled an arbitrarily anisotropic half-space and an arbitrarily anisotropic anomalous body embedded in an arbitrarily anisotropic rock. Through the analysis of the several numerical results, we come to conclusions as following:

1) The circular scanning measurement has advantages to recognize the characteristics of anisotropy. Comparing to the traditional measurement, the results of circular scanning measurement can clearly show the direction of anisotropic axis and apparent resistivity parameters.

2) There are apparent resistivity anisotropic paradoxes in the results of the circular scanning measurement. The anisotropic distribution characteristics of the surrounding rocks and the anomalous body can be distinguished by changing the offset.

ACKNOWLEDGMENTS

This paper is supported by National Nature Science Foundation of China (41530320, 41774125) and Key National Research Project of China (2016YFC0303100, 2017YFC0601900).

REFERENCES

Habberjam, G., 1975, Apparent Resistivity, Anisotropy and Strike Measurements: Geophysical Prospecting, 23, 211-247.

Jin, Jianming., 2014, The Finite Element Method in Electromagnetics: Xi'an University Press.

Li, P., Uren, N., 1997, Analytical Solution for the Point Source Potential in an Anisotropic 3-D Half-Space I: Two-Horizontal-Layer Case: Mathematical and Computer Modelling, 26, 9-27.

Li, P., Uren, N., 1998, The Modelling of Direct Current Electric Potential in an Arbitrarily Anisotropic Half-Space Containing a Conductive 3-D Body: Journal of Applied Geophysics, 38, 176-181.

Pain, C. C., *et al*., 2003, Anisotropic Resistivity Inversion: Inverse Problems, 19, 1081-1111.

Ren, Z., Tang, J., 2010, 3D direct current resistivity modeling with unstructured mesh by adaptive finite-element method: Geophysics, 75(1), 7-17.

Ren, Z., Tang, J., 2014, A Goal-Oriented Adaptive Finite-Element Approach for Multi-Electrode Resistivity System: Geophysical Journal International, 199, 136-145.

Si, H., 2006, A Quality Tetrahedral Mesh Generator and Three-Dimensional Delaunay Triangulator: Ph.D. Thesis, Weierstrass Institute for Applied Analysis and Stochastic.

Wait, J. R., 1990, Current Flow into a Three-Dimensionally Anisotropic Conductor: Radio Science, 25, 689-694.

Wang, Feiyan., 2009, 2.5-D DC Resistivity Modeling by the Adaptive Finite-Element Method with Unstructured Triangulation: M.S. Thesis, Central South University.

Wang, W., et al, 2013, Three-Dimensional DC Anisotropic Resistivity Modelling Using Finite Elements on Unstructured Grids: Geophysical Journal International, 193, 734-746.

Wang, T., Fang, S., 2001, 3-D Electromagnetic Anisotropy Modelling Using Finite Difference: Geophysics, 66, 1386-1398.

Xu, Shizhe, *et al*., 1994, The Finite Element Method for Solving Anomalous Potential for Resistivity Surveys: Chinese Journal of Geophysics, 37, 511-515.

Yin, C., Weidelt, P., 1999, Geoelectrical Fields in a Layered Earth with Arbitrary Anisotropy: Geophysics, 64, 426-434.

Yin, C., 2000, Geoelectrical Inversion for a One-Dimensional Anisotropic Model and Inherent Non-Uniqueness: Geophysical Journal International, 140, 11-23.

Yin, C., Maurer, H. M., 2001, Electromagnetic Induction in a Layered Earth with Arbitrary Anisotropy: Geophysics, 66, 1405-1416.

Yin, C., *et al*., 2016, Forward Modelling of Marine DC Resistivity Method for a Layered Anisotropic Earth: Applied Geophysics, 13, 279-287.

Zhou, B., Greenhalgh, M., & Greenhalgh, S., 2009, 2.5-d/3-d resistivity modelling in anisotropic media using Gaussian quadrature grids: Geophysical Journal International, 176, 63-80.

Zienkiewicz, O. C., Zhu, J. Z., 1992, Super-Convergent Patch Recovery and a Posteriori Error Estimates: Part1: The Recovery Technique: Internatioanl Journal for Numerical Methods in Engineering, 33, 1331-1364.